

Inversion Symmetry Breaking in Epitaxial Ultrathin Bi (111) Films

Hadass S. Inbar^{1*}, Muhammad Zubair^{2,3}, Jason T. Dong¹, Aaron N Engel¹, Connor P. Dempsey⁴, Yu Hao Chang¹, Shinichi Nishihaya^{1†}, Shoaib Khalid^{2,3}, Alexei V. Fedorov⁵, Anderson Janotti³, Chris J. Palmström^{1,4*}

¹*Materials Department, UC Santa Barbara, CA 93106*

²*Department of Physics and Astronomy, University of Delaware, Newark, DE 19716, USA*

³*Department of Materials Science and Engineering, University of Delaware, Newark, DE 19716, USA*

⁴*Department of Electrical & Computer Engineering, UC Santa Barbara, CA 93106*

⁵*Advanced Light Source, Lawrence Berkeley National Laboratory, Berkeley, CA 94720, USA*

(Dated: May 16, 2023)

Bismuth (Bi) films hold potential for spintronic devices and topological one-dimensional edge transport. Large-area high-quality (111) Bi ultrathin films are grown on InSb (111)B substrates. Strong film-substrate interactions epitaxially stabilize the (111) orientation and lead to inversion symmetry breaking. We resolve the longstanding controversy over the \mathbb{Z}_2 topological assignment of bismuth and show that the surface states are topologically trivial. Our results demonstrate that interfacial bonds prevent the semimetal-to-semiconductor transition predicted for freestanding bismuth layers, highlighting the importance of controlled functionalization and surface passivation in two-dimensional materials.

Corresponding authors

* Email: hadass@ucsb.edu (H.S.I.), cjpalm@ucsb.edu (C.J.P.)

Scientists have studied strain and quantum size effects in bismuth (Bi) (111) films for decades, which provide a rich platform for tuning topological order [1], semimetal to semiconducting transitions [2], and quantum-well states [3]. The low carrier density, long mean free path, large spin-orbit coupling, and presence of spin-polarized surface states [4] have made Bi films a promising system for future applications in spintronics [5]. Group-V elemental two-dimensional (2D) layers have also attracted interest in classical electronic and optoelectronic device applications due to their high carrier mobilities and potential bandgap tunability [6]. The large mass anisotropy in the surface state and the bulk band valleys in the band structure of Bi allow valley degeneracy to be controlled by the orientation of an applied magnetic field. This feature can be used in valleytronic devices which encode information through valley-polarized currents [7]. In the field of topological materials, there is an ongoing effort to classify the \mathbb{Z}_2 invariant of Bi experimentally [8–10], which also proves challenging to calculate computationally [11]. A single Bi (111) bilayer (BL) with a nontrivial \mathbb{Z}_2 topology is predicted to behave as a quantum spin Hall insulator [12]. Along the Bi (111) step edges, one-dimensional (1D) helical modes were also observed [13,14], an ingredient in one proposed platform to construct Majorana zero modes [15].

The synthesis of large-area single-domain ultrathin (<6 BL) buckled Bi (111) on conventional semiconducting substrates has remained a challenge, with only planar bismuthene wetting layers on SiC [16] and GaAs [17] reported thus far. On weakly interacting substrates, such as highly oriented pyrolytic graphite, Bi nucleates typically in the black phosphorus (BP)-like phase [18,19], and transforms later to the rhombohedral (111)_r oriented phase. In Si or Ge (111) substrates, weak film-substrate van der Waals (vdW) interactions [20,21] also lead to the nucleation of a nearly freestanding Bi layer, starting at the BP phase and transforming to a (111)_r orientation only after a 6-8 BL thick film coalesces [22]. Ultrathin Bi (111) films were nucleated on the topological insulator substrate Bi₂Te₃ [23–26], where in-plane contraction [27,28] is suggested to stabilize a topologically insulating phase. However, compressive strain and band hybridization with the Bi₂Te₃ substrate, along with low correspondence between the experimental data and the calculations at the ultrathin limit [24], make it difficult to study the topological classification of unstrained Bi and the semimetal to semiconducting transition predicted for ultrathin Bi films [29].

Bulk Bi is a low-carrier semimetal [Fig. 1, (a) and (b)] with a valence-band maximum at the time-reversal invariant momentum (TRIM) T point (projecting to $\bar{\Gamma}$ for the (111) surface) and a conduction-band minimum at the L TRIM point (projecting to \bar{M}). The small direct bandgap at the L point is only a few meV, and determines whether Bi is a strong topological insulator (TI, an inverted bandgap at L) or a higher-order topological insulator (HOTI, no band inversion at L). Bi is predicted to lie at the border of a topological phase transition between the HOTI and TI phases [9]. Yet despite

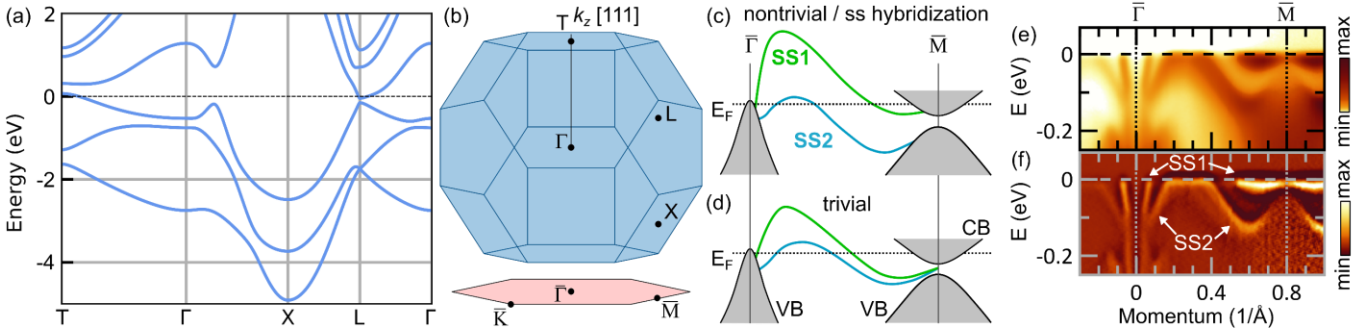


Fig. 1. (a) Calculated bulk band structure of Bi showing the hole and electron pockets at TRIM points T and L, respectively. (b) The bulk Brillouin zone and TRIM points projected onto the (111) surface Brillouin zone. (c) and (d) Schematic drawings of two possible surface state (SS1 and SS2) dispersions and projected valence and conduction bands (VB, CB) along $\bar{\Gamma} - \bar{M}$ (c) Connectivity of SS1 and SS2 with the CB and VB, respectively, at the \bar{M} point. The surface state gap could indicate either a topologically nontrivial band structure for a semi-infinite crystal or interactions between surface states at the top and bottom surfaces in a thin film. (d) Surface state degeneracy at \bar{M} , indicating a \mathbb{Z}_2 trivial band structure. (e and f) ARPES E - k dispersion of the surface states at $h\nu = 37.5$ eV for a 200 BL thick Bi (111) film grown on InSb (111)B presenting a very small/nonexistent gap at the \bar{M} point. (e) Raw data and the (f) curvature plot [30] of the raw data enhancing the dispersive features.

the challenge of estimating the gap size at the L point, most DFT calculations predict a trivial band order at the L point, with quasiparticle self-consistent GW calculations yielding a gap of 13 meV compared to 86 meV in standard DFT [1]. Calculations have shown that the indirect T-L gap and the inversion bandgap at L depend on electron doping [31], biaxial and shear strain [1,9,24], and bulk alloying in $\text{Bi}_{1-x}\text{Sb}_x$ [32].

ARPES measurements [8,33,34] of Bi thin films have nonetheless shown surface states gapped at \bar{M} , which in the past was attributed to a \mathbb{Z}_2 nontrivial band topology [Fig. 1(c)]. Since the surface states near the Brillouin-zone edge penetrate deep into the film bulk, on the order of 100s of BLs [11,35,36], crosstalk between surface states on neighboring surfaces could lead to the formation of a hybridization gap even in 200 BL [8] thick trivial semimetals [Fig. 1(c)] [11]. The bandgap at the L point is predicted to decrease monotonically with film thickness down to a finite trivial gap [11]. Therefore, a transition from an un-inverted to-inverted regime is not expected at the ultrathick limit unless external stimuli (such as strain or doping) are coupled to film thickness variations.

Recent *ab initio* calculations have predicted that in inversion a-symmetric films (resulting from surface perturbations/functionalization [37,38] or inter/intra-BL expansion [39]), one could more easily distinguish between the \mathbb{Z}_2 topologically trivial and nontrivial phases due to the emergence of degenerate surface states observed only from one surface, as schematically portrayed in Fig. 1(d). Surface state degeneracy at both $\bar{\Gamma}$ and \bar{M} leads to an even number of surface state Fermi surface contours between the TRIM points, resulting in a trivial \mathbb{Z}_2 topological assignment [32]. Thus, to study the true topological nature of Bi, a substrate/overlayer with strong bonding to Bi films is necessary to break inversion symmetry and prevent surface state hybridization, facilitating the topological phase assignment of Bi. In this work, we have identified a semiconducting substrate, InSb (111)B, satisfying this condition and allowing us to break inversion symmetry in epitaxial Bi films through strong film-substrate interactions. Unlike previously explored substrates, these strong interactions allow us to stabilize ultrathin (<6 BL) large-area Bi films in the (111) orientation down to 1 BL thick films while avoiding neighboring surface state hybridization.

Bi films are grown via molecular beam epitaxy (MBE, see Section S1 for details) on unintentionally doped InSb (111)B wafers. The films are then studied *in vacuo* with scanning tunneling microscopy (STM), reflection high energy diffraction (RHEED), and ARPES. Fig. 2 presents an overview of the nucleation conditions and structure of the Bi films grown on InSb (111)B. Fig. 2(a and b) shows the epitaxial relationship between the InSb (111)B surface and (111) $_r$ (0001) $_{\text{hex}}$ Bi. The (111) $_r$ rhombohedral notation of Bi can also be simplified using the (0001) $_{\text{hex}}$ quasi-hexagonal unit cell, where 3 BL (BL=3.95 Å) define the hexagonal out-of-plane lattice constant of $c_0=11.862$ Å, with an in-plane lattice constant $a_0=4.546$ Å [40]. Each Bi BL has a buckled structure with a vdW-like gap separating the BLs. The mismatch between the Bi bulk lattice constant and InSb <110> atomic spacing is small, with only 0.8% nominal biaxial tensile strain applied to the Bi film. RHEED patterns in Fig. 2(c) confirm the nucleation of smooth (1×1) unreconstructed Bi films on a well-ordered (3×3) InSb (111)B surface reconstruction. STM images in Fig. 2(d-g) show the evolution of the ultrathin film morphology with film thickness. In Fig. 2(d), an atomically smooth InSb (111)B starting surface is measured, with an atomic (3×3) surface reconstruction [Fig. 2(d), inset] consistent with previous observations [41].

Following the deposition of 1 BL, the Bi film evolves into a fractal Sierpiński triangle-like structure [Fig. 2(e)] which was recently reported for the same film-substrate system [41]. For Bi films with a 2-3 BL thickness, the fractal pattern transforms to a uniform coverage of Bi (111) with 1-2 BL steps and wetting layer patch areas. In Fig. 2(f), we observe only a single domain orientation in our STM images, unlike the common rotational domains seen thus far for thin Bi films [21]. The azimuthal alignment and in-plane strain are further studied with STM and X-ray diffraction [42],

where the epitaxial film-substrate relationship and film strain relaxation are monitored as a function of film thickness. It was shown that coherent strain is maintained in the film only up to 2 BL. Films thicker than 2 BL begin to partially relax and form a soliton network, a unique strain relief mechanism in vdW materials [43], observed in Bi films only when grown on InSb [41,42]. The relaxed soliton network is also evident in Fig. 2(g) for a 5.4 BL film. Bi films thicker than 30 BL are fully relaxed and present no biaxial strain in the topmost BL [42].

ARPES measurements of the surface states and quantum-well states in the Bi (111)/InSb (111)B films were conducted at the Advanced Light Source at 11 K (see Section S1 for details). Fig. 3(a) shows the Fermi surface of a 5.4 BL Bi film, presenting a dominant three-fold symmetry as the surface states disperse from the valence band at $\bar{\Gamma}$ towards \bar{M} , indicating a single epitaxial domain orientation and in agreement with the STM measurements. In Fig. 3(b-e), we follow the evolution of surface states (SS1 and SS2) and quantum-well states as a function of film thickness near \bar{M} , with the wide energy range scans provided in Fig. S1. Due to the small bulk carrier density, quantum confinement effects in Bi films persist for films 10s of BLs thick, leading to well-resolved subbands for all films thinner than 200 BL. Despite the ultrathin thickness of the Bi films studied (< 6 BL), we do not observe in ARPES any of the InSb valence band dispersions originating from the underlying substrate, as confirmed by examining a reference InSb (111)B surface in Fig. S2.

Contrary to earlier ARPES reports for Bi (111) grown on other substrates, such as Si(111) [3], Ge (111) [8], or Bi₂Te₃ (111) [24,26], we observe in Fig. 3(b and c) a distinct surface state band degeneracy at the \bar{M} point, consistent with the trivial surface state assignment of Bi [Fig. 1(d)] and indicative of the surface state bands avoiding crosstalk between the top and bottom surfaces. Ruling out the strong TI phase classification for Bi (111)/InSb(111)B suggests that the films should lie in the HOTI phase, though we do not detect any of the 1D edge state modes predicted for the HOTI phase [13], likely due to their relatively weak spectral weight [44]. For a Bi (111) film, 1D states would serpentine along $\langle \bar{1}2\bar{1}0 \rangle$ edges corresponding to the $\bar{\Gamma} - \bar{K}$ direction [14,44].

To elucidate the origin of the avoided hybridization of neighboring surface states, we perform DFT calculations for two possible Bi film structures with thicknesses varying from 1 to 6 BLs: (i) an inversion-symmetric freestanding Bi slab [Fig. 4(a)] and (ii) a Bi film on an InSb slab [Fig. 4(b), see Section S1 and Section S2 for details). Our band structure calculations for the freestanding Bi layers in Fig. 4C are consistent with earlier studies [29,45], predicting a semimetal to semiconductor transition for the thinnest 1 BL thick film and the two surface states gapped at \bar{M} . On the other hand, the Bi/InSb stack in Fig. 4(d) shows a surface state degeneracy at \bar{M} and an increasing separation in the surface state Fermi wavevectors with film thickness. These results for the Bi/InSb (111)B structure calculations agree with our experimental observations in Fig. 3(b-e) and Fig. S1.

The surface state crossing behavior in relatively thin films, which should be susceptible to surface state hybridization, can be explained by strong Bi-InSb interfacial bonding causing symmetry breaking. Bi films grown on other substrates have not exhibited band degeneracy at \bar{M} due to weak vdW-like interactions at the film-substrate interface [22]. Several experimental observations support the existence of strong Bi-InSb bonding. First, we note the epitaxial stabilization of ultrathin (111) Bi on InSb for films as thin as 1 BL in Fig. 2(e), and the formation of a unique fractal structure that requires strong Bi-InSb bonding [41]. Moreover, the nucleation of tensile-strained and azimuthally aligned Bi films [42] to the underlying InSb substrate suggests that the bonding energy initially surpasses the elastic energy later gained when the film relaxes. Finally, ultraviolet photoemission measurements reveal a shift in both the In 4d and Sb 4d core levels upon Bi deposition in Fig. S3, indicating the formation of Bi-Sb bonds and *p*-type Fermi level pinning of InSb at the interface. No In or Sb core levels were observed for films thicker than 5.4 BL, confirming layer-by-layer deposition and large-area uniform coverage of the ultrathin films.

To understand the nature of bonding between Bi and InSb, and whether remnant tensile biaxial strain could lead to a trivial L gap [1] and influence our topological phase assignment, we examined the degree of in-plane relaxation predicted by DFT calculations (Fig. S6 and Section S3) and compared the lattice parameters to experimental values [42]. The unstrained Bi/InSb structure reproduces the experimental trend of early film relaxation starting from 2 BLs [Fig.

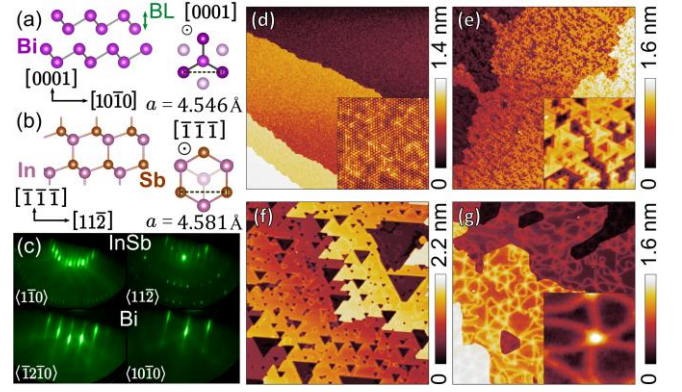


Fig. 2. Side and top-view models of (a) the Bi (0001)_{hex} surface illustrating intralayer covalent-like bonds and interlayer vdW stacking and (b) InSb (111)B unreconstructed surface. (c) RHEED patterns and epitaxial alignment of the (3×3) InSb (111)B substrate and (1×1) Bi (0001)_{hex} surface. (d-g) STM images of InSb and ultrathin Bi films 400×400 nm². (d) InSb (111)B substrate (bias voltage, V_b: 1.2 V), 20×20 nm² inset exhibits the atomic resolution of the (3×3) surface reconstruction (V_b: 1 V). (e) 1 BL Bi film (V_b: 3 V). 50×50 nm² inset depicts the fractal pattern (V_b: 3 V). (f) 2.6 BL Bi film, featuring continuous coverage above the percolation threshold; exposed patch area and density determined by annealing duration (V_b: 3 V). (g) 5.4 BL thick film, showing progressive film relaxation (V_b: 3 V); 50×50 nm² inset highlights a soliton node (V_b: 0.25 V).

2(f)] [42] and shows no significant change in the surface state dispersion or quantum-well energies, therefore our trivial \mathbb{Z}_2 topological assignment applies to Bi films with biaxial strain ranging from 0-0.8% tensile strain. DFT investigating the layer-resolved localization of the surface states (Fig. S7) revealed that for a \mathbb{Z}_2 trivial Bi film the surface states are heavily weighted only at the film-vacuum surface and have diminished presence at the InSb interface. Conversely, in the \mathbb{Z}_2 nontrivial case, the surface states at the top and bottom interfaces remain robust against substrate perturbations.

Another property affected by inversion-symmetry breaking and tensile strain in ultrathin Bi films is the predicted bandgap opening in a 1 BL Bi film [29,46]. According to earlier predictions, freestanding Bi films subjected to tensile strain should undergo a semimetal to semiconducting transition (indirect gap T-L) resulting in a valence-band edge displaced to higher binding energies and a lowered surface state minima at $\bar{\Gamma}$ [1,24,26,29,33,45]. However, our Bi/InSb DFT calculations show that the surface state crossing at $\bar{\Gamma}$ moves closer to the Fermi level as the film thickness decreases, both in Bi films that are tensile strained to the underlying InSb structure [Fig. 4(d)] and Bi films that relax above InSb (see Section S2). ARPES data in Fig. S4 show that the surface state crossing energy at $\bar{\Gamma}$ approaches the Fermi level as the film thickness decreases. A similar trend was observed for ultrathin Sb/InSb(111)A films [47]. Thus, film-substrate interactions at the few-BL limit could drive the valence band energy shift. Broken inversion symmetry in Fig. 4(d) also results in trivial surface states intersecting the Fermi level down to the ultrathin limit of a 1 BL thick film. Therefore, any 1D edge transport channel in the Bi HOTI phase will coexist with trivial surface state conduction unless both interfaces are passivated. Our DFT calculations are consistent with ARPES measurements of a 1.3 BL thick film (Fig. S5), showing the surface states transversing the Fermi level along $\bar{\Gamma} - \bar{M}$.

Next, we analyzed the extent of quantum confinement in the quantum-well states in Fig. 4(e) and Fig. S1 using a phase accumulation model [3,8,33], as detailed in Section S3. At a thickness of 200 BL, quantum-well states are not observed in Fig. 3(e) due to the small energy spacing, but thinner films display a larger quantum-well state energy separation with decreasing film thickness. The binding energies at \bar{M} of the top three quantum-well bands ($n=1$ being the surface state crossing point and $n=2,3$ the two following quantum-well states below) in the DFT calculations and ARPES measurements for varying Bi film thicknesses (N) are compared in Fig. 4(e), showing excellent agreement. For films thicker than 10 BLs, a linear-like region in Fig. 4(e) for band energy vs. inverse film thickness describes the

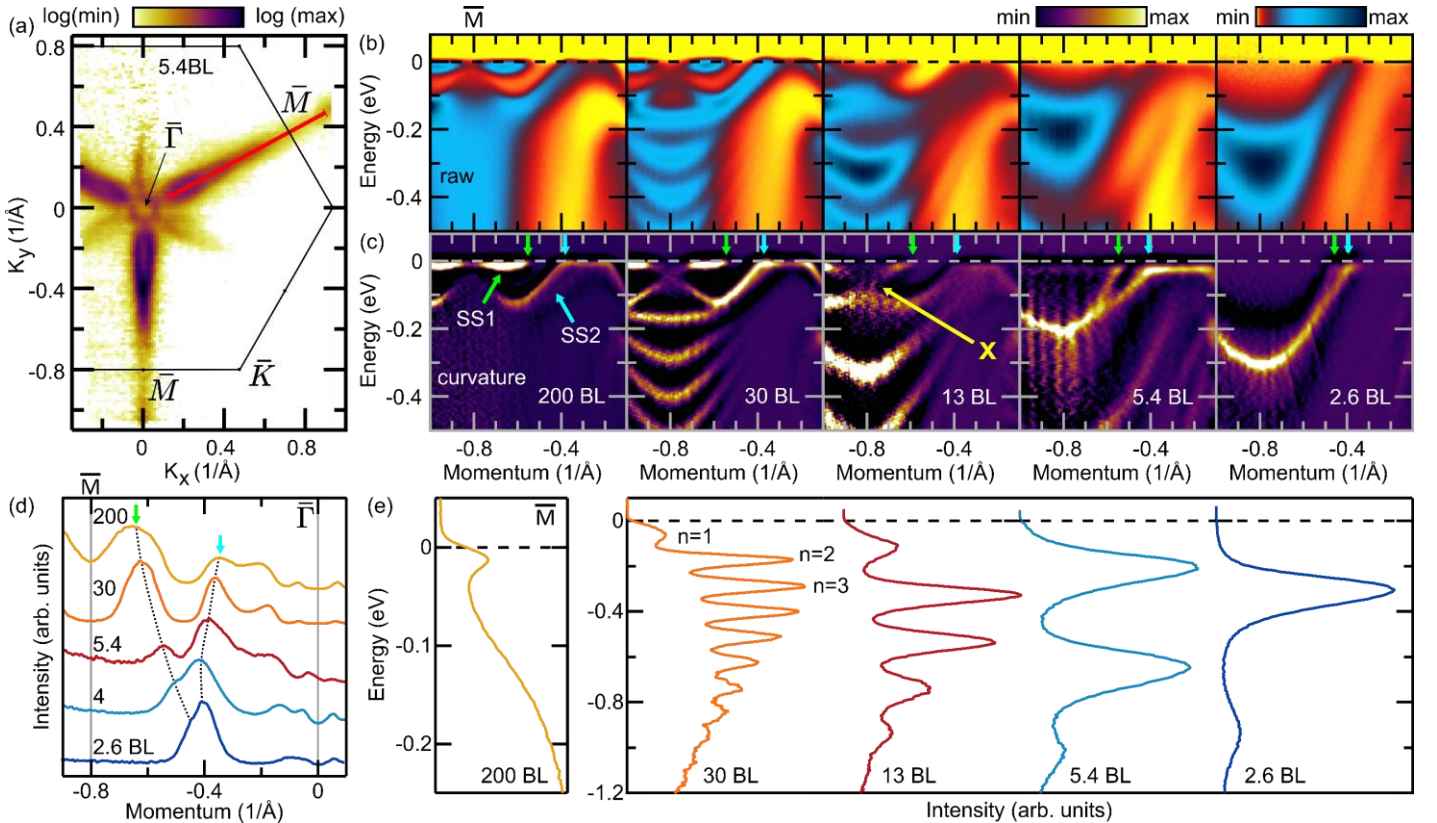


Fig. 3. Bi (111) surface states (SS1, SS2) and quantum-well states measured with ARPES at an incident photon energy $h\nu = 37.5$ eV for various film thicknesses. (a) Fermi surface of a 5.4 BL thick Bi (111) film at the Fermi energy, E_F . The corresponding $E-k$ cut along the $\bar{\Gamma} - \bar{M}$ path in (b) and (c) is highlighted. (b) ARPES raw images and (c) curvature plots enhancing the dispersive features. The surface state band degeneracy at \bar{M} ($k = 0.8 \text{ \AA}^{-1}$), marked by X, is observed due to inversion symmetry breaking. (d) Momentum distribution curves at E_F . The surface state Fermi level crossings near \bar{M} , highlighted by arrows in (c) and (d), decrease in separation as the films become thinner. (e) Energy distribution curves at the \bar{M} point showing the energies of the quantum-well states analyzed in Fig. 4(e).

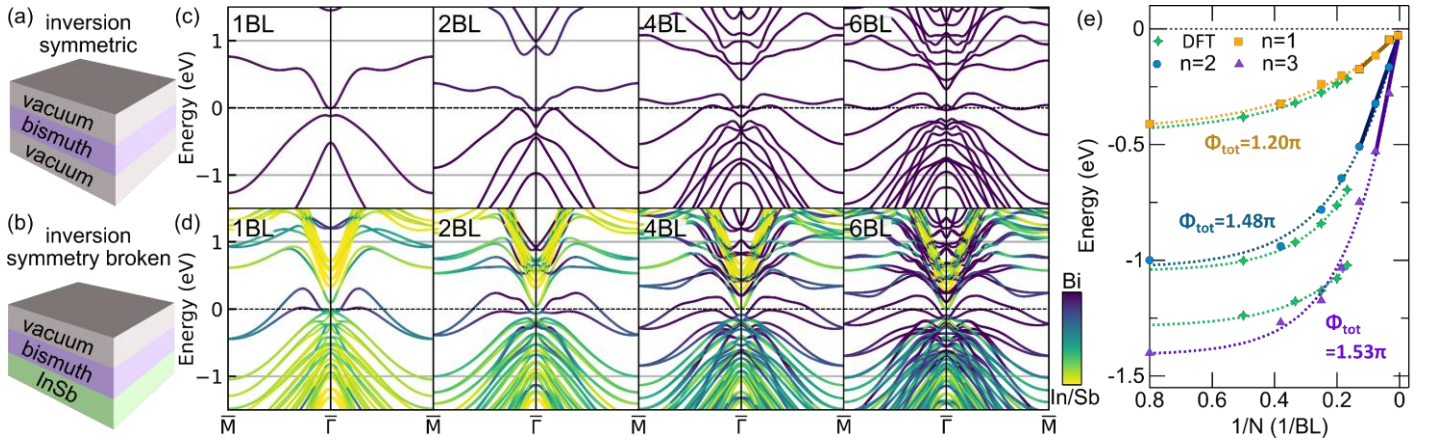


Fig. 4. Inversion symmetry breaking in ultrathin Bi films. Schematics of stacks for (a) a freestanding film preserving inversion symmetry and (b) a film with broken inversion symmetry. DFT calculations along $\bar{M} - \bar{\Gamma} - \bar{M}$ for varying ultrathin film thicknesses for (c) the freestanding Bi slab in (a) and (d) the film with broken inversion symmetry in (b). In (d), all states with more than 60% of their spectral weight in the Bi film are marked in purple, and states with 0% of their weight in the Bi film (originating from the InSb layer) are marked in yellow. (e) DFT (green) and ARPES (yellow, blue, purple) quantum-well state energy position at \bar{M} vs inverse film thickness, $1/N$. Full solid lines are linear fits used for analyzing the total phase shift (described in Section S3), and the dotted lines are drawn as guides for the eye.

expected E - k_z bulk-like film dispersion [8]. Ultrathin Bi films with less than 10 BL do not obey the linear relationship $E \propto \frac{1}{N}$, thus indicating a deviation from bulk-like dispersion along X - L [see Fig. 1, (a) and (b)] suggesting a transition to 2D-like behavior in ultrathin films. From the linear fits in Fig. 4(e), we extract the total phase shift, Φ_{tot} : $\Phi_{tot}^{n=1} = 1.20\pi$, $\Phi_{tot}^{n=2} = 1.48\pi$, $\Phi_{tot}^{n=3} = 1.53\pi$ and the phase shift at the InSb-Bi interface ($\Phi_{Bi-InSb}$) at a 0.15 eV binding energy: $\Phi_{Bi-InSb}^{n=1} = 1.33\pi$, $\Phi_{Bi-InSb}^{n=2} = 1.61\pi$, $\Phi_{Bi-InSb}^{n=3} = 1.66\pi$. The phase shift calculated for the surface state Bi band $n=1$ is close to the value reported for Bi films grown on Si [3], indicating a similar confining potential for the top surface state. For the $n=2,3$ quantum-well states, a less confining phase shift is measured. This suggests a gradual increase in the degree of spilling of the quantum-well state electron density into the underlying InSb substrate for higher quantum numbers.

In conclusion, we report the growth and evolution of surface state dispersion for large-area, single-domain oriented ultrathin films of Bi (111) synthesized on InSb (111)B. We find that strong film-substrate bonds stabilize ultrathin Bi films in the (111) orientation, offering a new route for the epitaxial growth and integration of other related topological systems, such as compressive strained Bi films and $\text{Bi}_{1-x}\text{Sb}_x$ 2D layers on insulating III-V substrates. For the first time in Bi films, we observe a surface state crossing at the \bar{M} point, a signature of inversion symmetry-breaking in the \mathbb{Z}_2 topological trivial phase. We studied quantum-well states through a phase accumulation model and showed a significant increase in 2D-like behavior for films thinner than 10 BL. Contrary to previous predictions of confinement- [29] or strain-induced semimetal to semiconductor transition [48] in freestanding Bi films, we find that for inversion-symmetry broken films the surface states cross the Fermi level for all thicknesses down to 1 BL.

Our work demonstrates experimentally the possibility of tailoring topological and trivial surface states in group-V ultrathin 2D layers through heteroepitaxial interfaces. Despite numerous theoretical studies on the surface chemistry of buckled Bi films [37,38,49] and other elemental 2D materials [50], there are still few experimental reports on inorganic or molecular functionalization. Future attempts to control surface terminations in 2D materials through overlayer growth could aid in band structure engineering of inversion-symmetric structures and in identifying topological phases and their transport signatures in inversion-symmetric / a-symmetric films. A wide range of possibilities is now open for exploring wafer-scale ultrathin Bi/ $\text{Bi}_{1-x}\text{Sb}_x$ films of high crystalline quality for topological edge-transport studies and electronic and optoelectronic device applications.

REFERENCES

- [1] I. Aguilera, C. Friedrich, and S. Blügel, Phys. Rev. B **91**, 125129 (2015).
- [2] V. Sandomirskiĭ, Sov. J. Exp. Theor. Phys. **25**, 101 (1967).
- [3] T. Hirahara, T. Nagao, I. Matsuda, G. Bihlmayer, E. V. Chulkov, Y. M. Koroteev, and S. Hasegawa, Phys. Rev. B **75**, 035422 (2007).
- [4] A. Takayama, T. Sato, S. Souma, T. Oguchi, and T. Takahashi, Nano Lett. **12**, 1776 (2012).
- [5] P. Hofmann, Prog. Surf. Sci. **81**, 191 (2006).
- [6] Z. Wu and J. Hao, Npj 2D Mater. Appl. **4**, 4 (2020).
- [7] H. Du, X. Sun, X. Liu, X. Wu, J. Wang, M. Tian, A. Zhao, Y. Luo, J. Yang, B. Wang, and J. G. Hou, Nat. Commun. **7**, 10814 (2016).
- [8] S. Ito, B. Feng, M. Arita, A. Takayama, R.-Y. Liu, T. Someya, W.-C. Chen, T. Iimori, H. Namatame, M. Taniguchi, C.-M.

- Cheng, S.-J. Tang, F. Komori, K. Kobayashi, T.-C. Chiang, and I. Matsuda, *Phys. Rev. Lett.* **117**, 236402 (2016).
- [9] A. K. Nayak, J. Reiner, R. Queiroz, H. Fu, C. Shekhar, B. Yan, C. Felser, N. Avraham, and H. Beidenkopf, *Sci. Adv.* **5**, 37 (2019).
- [10] Y. Fukushima, K. Kawaguchi, K. Kuroda, M. Ochi, H. Tanaka, A. Harasawa, T. Iimori, Z. Zhao, S. Tani, K. Yaji, S. Shin, F. Komori, Y. Kobayashi, and T. Kondo, *ArXiv: 2303.17816* 1 (2023).
- [11] I. Aguilera, H.-J. Kim, C. Friedrich, G. Bihlmayer, and S. Blügel, *Phys. Rev. Mater.* **5**, L091201 (2021).
- [12] S. Murakami, *Phys. Rev. Lett.* **97**, 236805 (2006).
- [13] F. Schindler, Z. Wang, M. G. Vergniory, A. M. Cook, A. Murani, S. Sengupta, A. Y. Kasumov, R. Deblock, S. Jeon, I. Drozdov, H. Bouchiat, S. Guéron, A. Yazdani, B. A. Bernevig, and T. Neupert, *Nat. Phys.* **14**, 918 (2018).
- [14] I. K. Drozdov, A. Alexandradinata, S. Jeon, S. Nadj-Perge, H. Ji, R. J. Cava, B. Andrei Bernevig, and A. Yazdani, *Nat. Phys.* **10**, 664 (2014).
- [15] B. Jäck, Y. Xie, J. Li, S. Jeon, B. A. Bernevig, and A. Yazdani, *Science* **364**, 1255 (2019).
- [16] F. Reis, G. Li, L. Dudy, M. Bauernfeind, S. Glass, W. Hanke, R. Thomale, J. Schäfer, and R. Claessen, *Science* **357**, 287 (2017).
- [17] Y. Liu, S. Benter, C. S. Ong, R. P. Maciel, L. Björk, A. Irish, O. Eriksson, A. Mikkelsen, and R. Timm, *ACS Nano* **17**, 5047 (2023).
- [18] P. J. Kowalczyk, O. Mahapatra, D. N. McCarthy, W. Kozłowski, Z. Klusek, and S. A. Brown, *Surf. Sci.* **605**, 659 (2011).
- [19] S. A. Scott, M. V. Kral, and S. A. Brown, *Surf. Sci.* **587**, 175 (2005).
- [20] E. S. Walker, S. R. Na, D. Jung, S. D. March, J.-S. Kim, T. Trivedi, W. Li, L. Tao, M. L. Lee, K. M. Liechti, D. Akinwande, and S. R. Bank, *Nano Lett.* **16**, 6931 (2016).
- [21] T. Shirasawa, M. Ohyama, W. Voegeli, and T. Takahashi, *Phys. Rev. B* **84**, 075411 (2011).
- [22] T. Nagao, J. Sadowski, M. Saito, S. Yaginuma, Y. Fujikawa, T. Kogure, T. Ohno, Y. Hasegawa, S. Hasegawa, and T. Sakurai, *Phys. Rev. Lett.* **93**, 105501 (2004).
- [23] T. Hirahara, G. Bihlmayer, Y. Sakamoto, M. Yamada, H. Miyazaki, S. Kimura, S. Blügel, and S. Hasegawa, *Phys. Rev. Lett.* **107**, 166801 (2011).
- [24] T. Hirahara, N. Fukui, T. Shirasawa, M. Yamada, M. Aitani, H. Miyazaki, M. Matsunami, S. Kimura, T. Takahashi, S. Hasegawa, and K. Kobayashi, *Phys. Rev. Lett.* **109**, 227401 (2012).
- [25] F. Yang, L. Miao, Z. F. Wang, M. Y. Yao, F. Zhu, Y. R. Song, M. X. Wang, J. P. Xu, A. V. Fedorov, Z. Sun, G. B. Zhang, C. Liu, F. Liu, D. Qian, C. L. Gao, and J. F. Jia, *Phys. Rev. Lett.* **109**, 1 (2012).
- [26] L. Miao, M.-Y. Yao, W. Ming, F. Zhu, C. Q. Han, Z. F. Wang, D. D. Guan, C. L. Gao, C. Liu, F. Liu, D. Qian, and J.-F. Jia, *Phys. Rev. B* **91**, 205414 (2015).
- [27] N. Fukui, T. Hirahara, T. Shirasawa, T. Takahashi, K. Kobayashi, and S. Hasegawa, *Phys. Rev. B* **85**, 115426 (2012).
- [28] T. Shirasawa, J. Tsunoda, T. Hirahara, and T. Takahashi, *Phys. Rev. B* **87**, 075449 (2013).
- [29] Y. M. Koroteev, G. Bihlmayer, E. V. Chulkov, and S. Blügel, *Phys. Rev. B* **77**, 045428 (2008).
- [30] P. Zhang, P. Richard, T. Qian, Y.-M. Xu, X. Dai, and H. Ding, *Rev. Sci. Instrum.* **82**, 043712 (2011).
- [31] K.-H. Jin, H. W. Yeom, and F. Liu, *Phys. Rev. B* **101**, 035111 (2020).
- [32] L. Fu and C. L. Kane, *Phys. Rev. B* **76**, 045302 (2007).
- [33] S. Ito, M. Arita, J. Haruyama, B. Feng, W.-C. Chen, H. Namatame, M. Taniguchi, C.-M. Cheng, G. Bian, S.-J. Tang, T.-C. Chiang, O. Sugino, F. Komori, and I. Matsuda, *Sci. Adv.* **6**, 1 (2020).
- [34] Y. Ohtsubo, L. Perfetti, M. O. Goerbig, P. Le Fèvre, F. Bertran, and A. Taleb-Ibrahimi, *New J. Phys.* **15**, 033041 (2013).
- [35] K. Saito, H. Sawahata, T. Komine, and T. Aono, *Phys. Rev. B* **93**, 041301 (2016).
- [36] Y. Ohtsubo and S. Kimura, *New J. Phys.* **18**, 123015 (2016).
- [37] T.-R. Chang, Q. Lu, X. Wang, H. Lin, T. Miller, T.-C. Chiang, and G. Bian, *Crystals* **9**, 510 (2019).
- [38] I. N. Yakovkin, *J. Phys. Chem. Solids* **129**, 277 (2019).
- [39] M. Alcantara-Ortigoza and T. S. Rahman, 1 (2020).
- [40] H. Mönig, J. Sun, Y. M. Koroteev, G. Bihlmayer, J. Wells, E. V. Chulkov, K. Pohl, and P. Hofmann, *Phys. Rev. B* **72**, 085410 (2005).
- [41] C. Liu, Y. Zhou, G. Wang, Y. Yin, C. Li, H. Huang, D. Guan, Y. Li, S. Wang, H. Zheng, C. Liu, Y. Han, J. W. Evans, F. Liu, and J. Jia, *Phys. Rev. Lett.* **126**, 176102 (2021).
- [42] J. T. Dong, Unpublished (n.d.).
- [43] A. Kushima, X. Qian, P. Zhao, S. Zhang, and J. Li, *Nano Lett.* **15**, 1302 (2015).
- [44] A. Takayama, T. Sato, S. Souma, T. Oguchi, and T. Takahashi, *Phys. Rev. Lett.* **114**, 066402 (2015).
- [45] G. Cantele and D. Ninno, *Phys. Rev. Mater.* **1**, 014002 (2017).
- [46] Z.-Q. Huang, F.-C. Chuang, C.-H. Hsu, Y.-T. Liu, H.-R. Chang, H. Lin, and A. Bansil, *Phys. Rev. B* **88**, 165301 (2013).
- [47] B. Liu, T. Wagner, S. Enzner, P. Eck, M. Kamp, G. Sangiovanni, and R. Claessen, (2022).
- [48] C. König, J. C. Greer, and S. Fahy, *Phys. Rev. B* **104**, 035127 (2021).
- [49] C. König, J. C. Greer, and S. Fahy, *Phys. Rev. B* **104**, 045432 (2021).
- [50] A. J. Mannix, B. Kiraly, M. C. Hersam, and N. P. Guisinger, *Nat. Rev. Chem.* **1**, 0014 (2017).
- [51] J. T. Dong, H. S. Inbar, M. Pendharkar, T. A. J. van Schijndel, E. C. Young, C. P. Dempsey, and C. J. Palmstrøm, *ArXiv:2302.09234* (2023).
- [52] S. Cho, Y.-H. Um, Y. Kim, G. K. L. Wong, J. B. Ketterson, and J.-I. Hong, *J. Vac. Sci. Technol. A Vacuum, Surfaces, Film.* **20**, 1191 (2002).
- [53] J. Wever, H. L. Meyerheim, W. Moritz, V. Jahns, D. Wolf, H. Schulz, L. Seehofer, and R. L. Johnson, *Surf. Sci.* **321**, L225 (1994).
- [54] G. Kresse and J. Hafner, *Phys. Rev. B* **47**, 558 (1993).

- [55] G. Kresse and J. Hafner, Phys. Rev. B **49**, 14251 (1994).
- [56] J. P. Perdew, K. Burke, and M. Ernzerhof, Phys. Rev. Lett. **77**, 3865 (1996).
- [57] U. Herath, P. Tavadze, X. He, E. Bousquet, S. Singh, F. Muñoz, and A. H. Romero, Comput. Phys. Commun. **251**, 107080 (2020).
- [58] S. Ito, B. Feng, M. Arita, T. Someya, W.-C. Chen, A. Takayama, T. Iimori, H. Namatame, M. Taniguchi, C.-M. Cheng, S.-J. Tang, F. Komori, and I. Matsuda, Phys. Rev. B **97**, 155423 (2018).
- [59] L. Ö. Olsson, J. Kanski, L. Ilver, C. B. M. Andersson, M. Björkqvist, M. Göthelid, U. O. Karlsson, and M. C. Håkansson, Phys. Rev. B **50**, 18172 (1994).
- [60] C. L. Littler and D. G. Seiler, Appl. Phys. Lett. **46**, 986 (1985).
- [61] V. Hinkel, L. Sorba, and K. Horn, Surf. Sci. **194**, 597 (1988).
- [62] J. Heyd, G. E. Scuseria, and M. Ernzerhof, J. Chem. Phys. **118**, 8207 (2003).
- [63] J. Heyd, G. E. Scuseria, and M. Ernzerhof, J. Chem. Phys. **124**, 219906 (2006).
- [64] N. V. Smith, Phys. Rev. B **32**, 3549 (1985).
- [65] M. Milun, P. Pervan, and D. P. Woodruff, Reports Prog. Phys. **65**, 99 (2002).
- [66] T.-C. Chiang, Surf. Sci. Rep. **39**, 181 (2000).
- [67] L. Apker, E. Taft, and J. Dickey, Phys. Rev. **76**, 270 (1949).

Acknowledgments

Funding: Initial growth studies, ARPES experiments, and theoretical work were supported by the U.S. Department of Energy (contract no. DE-SC0014388). This research used resources of the Advanced Light Source, which is a DOE Office of Science User Facility under contract no. DE-AC02-05CH11231. We acknowledge the use of shared facilities of the NSF Materials Research Science and Engineering Center (MRSEC) at the University of California Santa Barbara (DMR 1720256). DFT calculations used the National Energy Research Scientific Computing Center (NERSC), a U.S. Department of Energy Office of Science User Facility operated under contract no. DE-AC02-05CH11231. H. S. I. gratefully acknowledges support from the UC Santa Barbara NSF Quantum Foundry funded via the Q-AMASE-i program under award DMR-1906325 and support for further growth studies and development of the vacuum suitcases.

Author contributions: H.S.I. and C.J.P. conceived the study. H.S.I. performed thin film growth, ARPES measurements, and data analysis. J.T.D. performed STM measurements with assistance from C.P.D. . A.N.E., Y.C., S.N., and A.V.F. assisted in ARPES experiments. DFT calculations were conducted by M.Z. under the supervision of S.K. and A.J. The authors thank Dai Q. Ho for useful discussions. A.N.E. and C.P.D. designed ultra-high vacuum components and sample holders. The manuscript was prepared by H.S.I. All authors discussed the results and commented on the manuscript.

Competing interests: The authors declare that they have no competing interests. **Data and materials availability:** All data needed to evaluate the conclusions in the paper are present in the paper and/or the Supplementary Materials. Additional data related to this paper may be requested from the authors.

Supplementary Materials for

Inversion Symmetry Breaking in Epitaxial Ultrathin Bi (111) Films

Hadass S. Inbar *et al.*

*Corresponding authors. Email: hadass@ucsb.edu (H.S.I.), cjpalm@ucsb.edu (C.J.P.)

Section S1: MBE thin film growth,

Section S2: Additional photoemission spectra and DFT calculations - Bi films and InSb substrate

Section S3: Phase accumulation model

Fig. S1 to S7

Table S1

References (51-67)

Section S1

MBE film growth

A well-ordered (3×3) surface of unintentionally doped epi-ready InSb (111)B wafers (Wafer Technology Ltd.) was prepared with atomic hydrogen cleaning for native oxide removal and was studied *in-vacuo* with STM [51]. The starting (111)B face was selected due to previous reports predicting improved wetting over InSb (111)A [52]. Layer-by-layer growth was observed for Bi nucleated both on the InSb (3×3) In-rich and (2×2) Sb-rich surface reconstructions, with a (3×3) reconstruction selected in this study to avoid unintentional Sb doping of the Bi film [53].

The thin Bi (111) films were grown by MBE in a modified Veeco Gen II growth chamber with a base pressure $<1\times 10^{-10}$ Torr. Bi was evaporated from an effusion cell with a deposition rate of 1.9×10^{14} atoms/cm²min, determined by Rutherford backscattering spectrometry measurements of the elemental area atomic density of calibration samples grown on Si. The nominal thickness is represented in units of bilayers (BLs), where 1 BL corresponds to the atom density in (111) planes assuming lattice matching to the underlying InSb substrate ($a_{\text{Bi}}^{\text{InSb}}=4.582\text{\AA}$): 1.10×10^{15} atoms/cm². Thin films are nucleated at 14 °C followed by low-temperature annealing at 80-120 °C for several hours to allow local ordering of the Bi atoms (confirmed by RHEED and STM) but avoid film dewetting observed at higher temperatures. The surface crystal quality was monitored *in situ* with RHEED during film growth and post-annealing. The samples were transferred *in vacuo* for ARPES and STM measurements and were eventually capped with a 5-nm-thick AlO_x layer deposited by electron-beam evaporation of Al₂O₃ source material to prevent film oxidation and dewetting when loading out of ultrahigh-vacuum for *ex situ* characterization. Lattice parameters, film thickness, and crystallinity information were extracted from high-resolution x-ray diffraction [42] and confirmed that the films have high crystalline ordering and sharp interfaces.

ARPES and STM measurements

The Advanced Light Source ARPES measurements were acquired with a Scienta DA30L hemispherical analyzer and were performed on *in vacuo* transferred samples, where a custom-built vacuum suitcase with a base pressure $<10^{-10}$ Torr was used to transfer films from the growth chamber at UC, Santa Barbara, to beamline 10.0.1.2 at the ALS in Berkeley. A *In vacuo* STM was performed with an Omicron LT STM at 77 K with a base pressure $<4\times 10^{-11}$ Torr.

First-principles calculations

We investigated the electronic structure of Bi thin films with DFT-based first-principles calculations with the projector augmented wave (PAW) method as implemented in the VASP code [54,55]. The generalized gradient approximation (GGA) of Perdew-Burke-Ernzerhof (PBE) for the exchange-correlation functional was used [56], including spin-orbit coupling as implemented in the VASP code. We used PAW potentials for Bi with five valence electrons, $6s^26p^3$, three valence electrons for In, $5s^25p^1$, and five valence electrons for Sb, $5s^25p^3$. For convergence of the electronic self-consistent calculations, a total energy difference criterion was defined as 10^{-6} eV. A cutoff energy of 500 eV is used in the plane wave basis set, and a Γ -centered $8\times 8\times 1$ k-point mesh was employed in the slab calculations. The calculations for bulk Bi were performed using the primitive rhombohedral cell with 2 atoms and a Γ -centered $12\times 12\times 12$ k-point mesh. The optimized lattice parameters of the primitive rhombohedral cell correspond to an in-plane lattice parameter $a_{\text{Bi}}^{\text{bulk}} = 4.523\text{\AA}$ and an out-of-plane lattice parameter $c_{\text{Bi}}^{\text{bulk}} = 3(d_{\text{vdW}} + d_{\text{BL}}) = 11.75\text{\AA}$ for the conventional hexagonal cell containing 6 atoms (where the interlayer vdW-like gap is: $d_{\text{vdW}} = 2.308\text{\AA}$ and the intralayer BL height is: $d_{\text{BL}} = 1.609\text{\AA}$).

Freestanding Bi layers and Bi/InSb structures were modeled with varying numbers of Bi BLs, from 1 to 6 BL. The lattice parameter of the 1-6 BL freestanding Bi films in Fig. 4(c) is fixed to the in-plane relaxed lattice parameter of bulk Bi: $a_{\text{Bi},\text{fixed}}^{\text{freestanding}} = 4.523\text{\AA}$. To study the effect of Bi ultrathin films on InSb substrate, we modeled the same varying number of Bi BLs on a 2-unit cell thick InSb (111)B slab with a vacuum thickness of 15\AA . The top surface of the InSb (111) slab (B face) was an unreconstructed Sb-polar layer, and the In atoms at the bottom surface (A face) were passivated with hydrogen with a $5/4$ fractional charge to fulfill 2 electrons per bond. The structures are relaxed vertically while keeping the in-plane lattice parameter fixed. The Bi/InSb structures with varying Bi layer thicknesses were constrained to the underlying InSb substrate lattice parameter $a_{\text{Bi},\text{fixed}}^{\text{Bi/InSb}} = a_{[110]}^{\text{InSb}} = 4.628\text{\AA}$, shown in Fig. 4D. In Section S2 we provide further details on (i) the band structure calculations for fully relaxed in-plane freestanding Bi and Bi/InSb, (ii) the top and bottom BL-resolved calculations for trivial and nontrivial band structures, and (iii) the stacking arrangement of Bi with respect to InSb. All the band structures were plotted using the PyProcar package [57].

Section S2

Photoemission spectra of the Bi films and InSb substrate

In Fig. S1, four Fermi-level band crossings are observed along $\bar{M} - \bar{\Gamma}$, twice for each surface state band highlighted in Fig. 1. An additional set of surface state bands [58] is centered at the $\bar{\Gamma}$ point near 0.2-0.6 eV with a crossing marked by X in Fig. S1. The valence bulk bands at the T and L high-symmetry points were not detected for any of the Bi films over an energy range of 18-60 eV in Fig. 1, Fig. S1, Fig. S4, and Fig. S5 owing to their low cross section compared to the surface states. As the surface states (crossing the Fermi level) disperse towards \bar{M} , additional quantum-well states are observed due to the hybridization of the surface states with the quantum-well states originating from the bulk band (and additional bulk quantum-well states are also apparent at the $\bar{\Gamma}$ point).

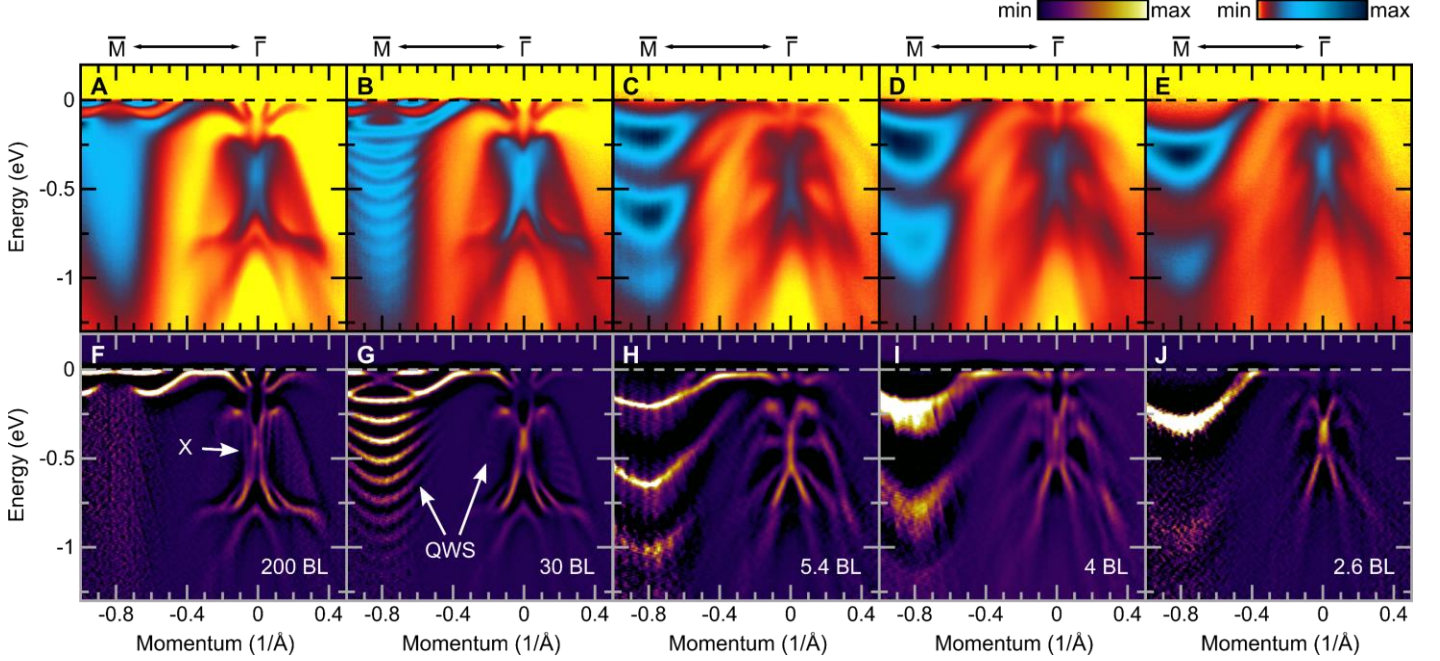


Fig. S1. ARPES spectra of Bi films along $\bar{M} - \bar{\Gamma}$ over a wide energy range. ARPES images of the raw spectra (A-E) and 2D curvature plots (F-J), enhancing the dispersive band features. Quantum-well states (QWS) and the crossing of the second pair of surface states at ~ 0.5 eV, marked by X, are highlighted. The spectra are measured at an incident photon energy $h\nu = 37.5$ eV.

Fig. S2 shows reference ARPES images for the atomic hydrogen-cleaned InSb (111)B substrate, collected at the two photon energies and E - k cut directions used for studying the Bi ultrathin films. We observe bulk valence bands and surface shadow bands due to the (3×3) surface reconstruction (resulting in the folding of the surface Brillouin zone, as shown in Fig. S2A). At $h\nu = 37.5$ eV (Fig. S2, C and D), there is a resonant enhancement of the valence band photoemission cross-section due to the proximity in energy to the Sb $4d \rightarrow 5p$ (valence band) transition (see Fig. S3), also leading to a stronger intensity of the shadow bands. While the photon energies of 37.5 and 20 eV should reflect cuts near the bulk Γ and L points [59] (see Fig. S2B), respectively, the valence band dispersion remains essentially unchanged, with the addition of bands centered at L for the 20 eV scans, indicating high k_z broadening. The InSb bands in Fig. S2 are not apparent in any of the Bi film ARPES measurements. Since InSb has a finite bandgap of 0.235 eV [60], the valence band maximum in Fig. S2 was set to the Fermi level position as it was shown in scanning tunneling spectroscopy measurements that the Fermi level of the (3×3) InSb (111)B surface is pinned near the valence band edge [51]. However, based on Bi/InSb Fermi level calibrations, the Fermi level position is likely 0.17 eV above the valence band maximum, which also yielded better agreement with literature values of InSb photoemission core level binding energies [61] (see Fig. S3C-D).

Fig. S3 presents the ultraviolet core-level photoemission spectra collected as a function of the Bi film thickness tracing the Bi $5d_{5/2}$, Sb $4d$, and In $4d$ core levels. A survey scan of the 1.3 BL film in Fig. S3A shows Bi $5d$ core levels with an intensity order of magnitude higher than the In and Sb-related peaks. The quenched intensity of the Sb and In core levels following the growth of just a few Bi BLs highlights the smooth InSb starting surface and the layer-by-layer growth of the Bi film. In Fig. S3B, the 1.3 BL Bi $5d_{5/2}$ peak presents additional components at a higher binding energy, either due to Bi-Sb bonds forming at the Bi-InSb (111)B interface or due to surface components related to Bi atoms with dangling bonds on the fractal-like surface (see Fig. 2). Upon increasing Bi film thickness, the Bi lineshape evolves into the bulk-like core level spectra with no pronounced change in the Bi core level binding energy. In Fig. S3C, a single In

4d core level bulk component is used to fit the InSb substrate spectra (In $4d_{5/2}$ = 17.18 eV and In $4d_{3/2}$ = 18.01 eV), and upon Bi deposition, a gradual decrease in binding energies is observed as the Bi film thickness increases. This shift in the In 4d spectra could be related to In-Bi bonds forming and/or band-bending in InSb (*p*-type like Fermi level pinning at the Bi-InSb interface). In Fig. S3D, two Sb 4d core level components are used to fit the InSb spectra: Sb $4d_{5/2}$ = 31.38 eV, 31.58 eV, and Sb $4d_{3/2}$ = 32.82 eV, 32.62 eV in agreement with previous photoemission measurements [61]. A sharp jump in the Sb 4d binding energy occurs upon Bi deposition. This shift could result from Sb-Bi bonds forming at the Bi-InSb interface. Similar to In 4d, the Sb core level binding energies decrease with increasing Bi film thickness, indicating *p*-type Fermi level pinning at the Bi-InSb interface.

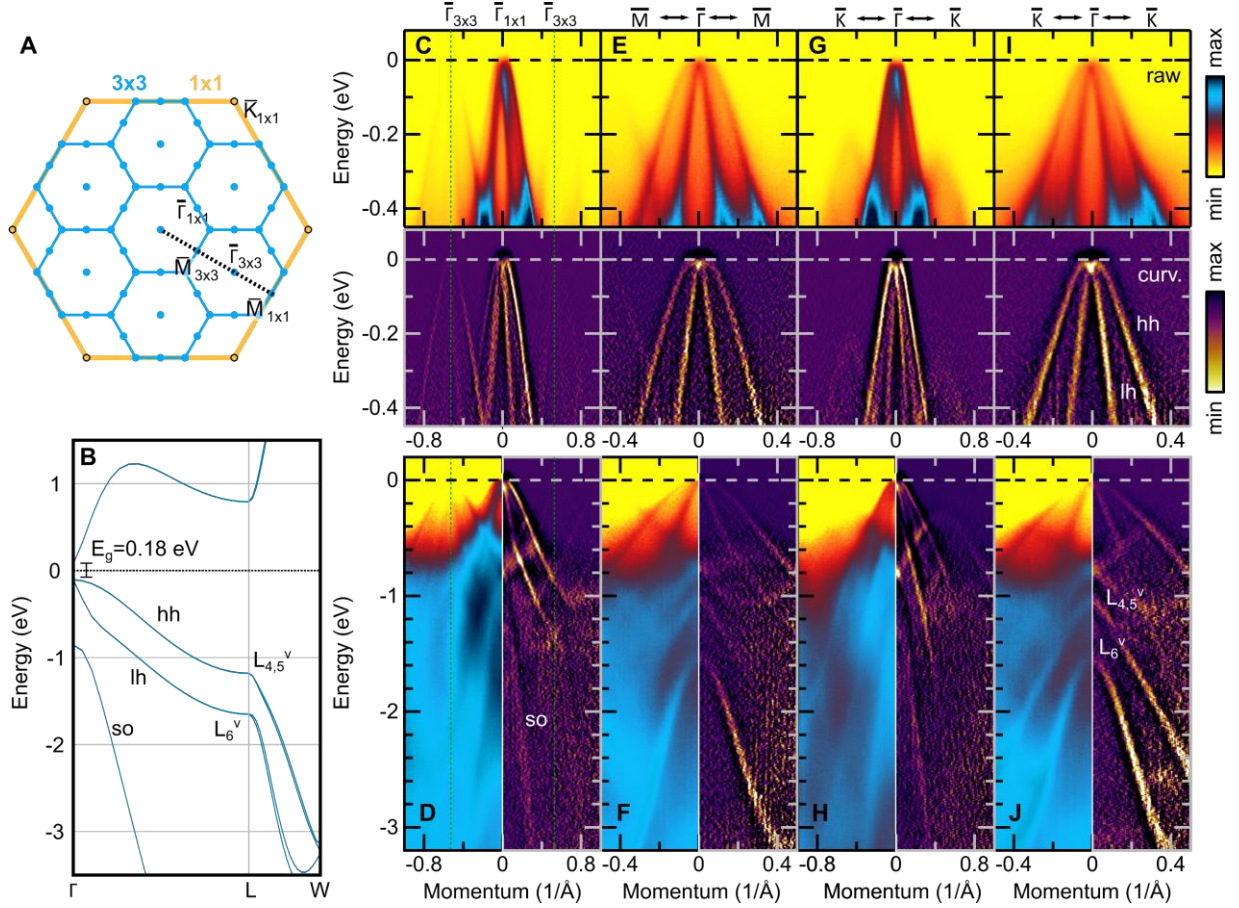


Fig. S2. InSb surface and bulk band structure and ARPES spectra. (A) Surface Brillouin zone and symmetry points of the (1x1) unreconstructed (orange) and (3x3) reconstructed surface (blue) of InSb (111)B. (B) HSE06-calculated band structure of InSb showing the heavy-hole (hh), light-hole (lh), and split-off (so) bands. (C-J) ARPES images of the raw spectra (top/left panels) and 2D curvature plots, enhancing the dispersive band features (bottom/right panels). (C-D) $\bar{M} - \bar{\Gamma} - \bar{M}$ cuts collected at an incident photon energy $h\nu = 37.5$ eV for (C) narrow and (D) wide energy ranges. Shadow bands due to the (3x3) surface reconstruction are marked by green lines. (E-F) $\bar{M} - \bar{\Gamma} - \bar{M}$ cuts at an incident photon energy $h\nu = 20$ eV for (E) narrow and (F) wide energy ranges. (G-H) $\bar{K} - \bar{\Gamma} - \bar{K}$ cuts at an incident photon energy $h\nu = 37.5$ eV for (G) narrow and (H) wide energy ranges. (I-J) $\bar{K} - \bar{\Gamma} - \bar{K}$ cuts at an incident photon energy $h\nu = 20$ eV for (I) narrow and (J) wide energy ranges.

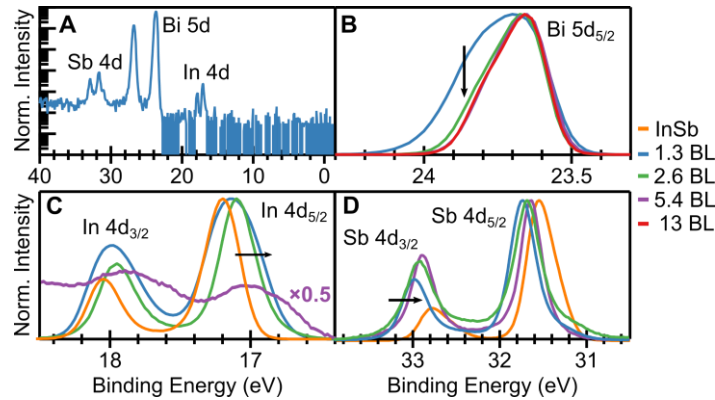


Fig. S3. Bi-InSb interfacial bonding revealed by core level photoemission for different Bi film thicknesses. Ultraviolet photoemission scans collected for the InSb (111)B (3x3) surface and Bi thin films with varying thicknesses. (A) Log-scale survey spectrum of the 1.3 BL Bi film collected at 80 eV. Photoemission spectra of (B) Bi $5d_{5/2}$ measured at 80 eV, (C) In 4d at 50 eV, and (D) Sb 4d at 80 eV.

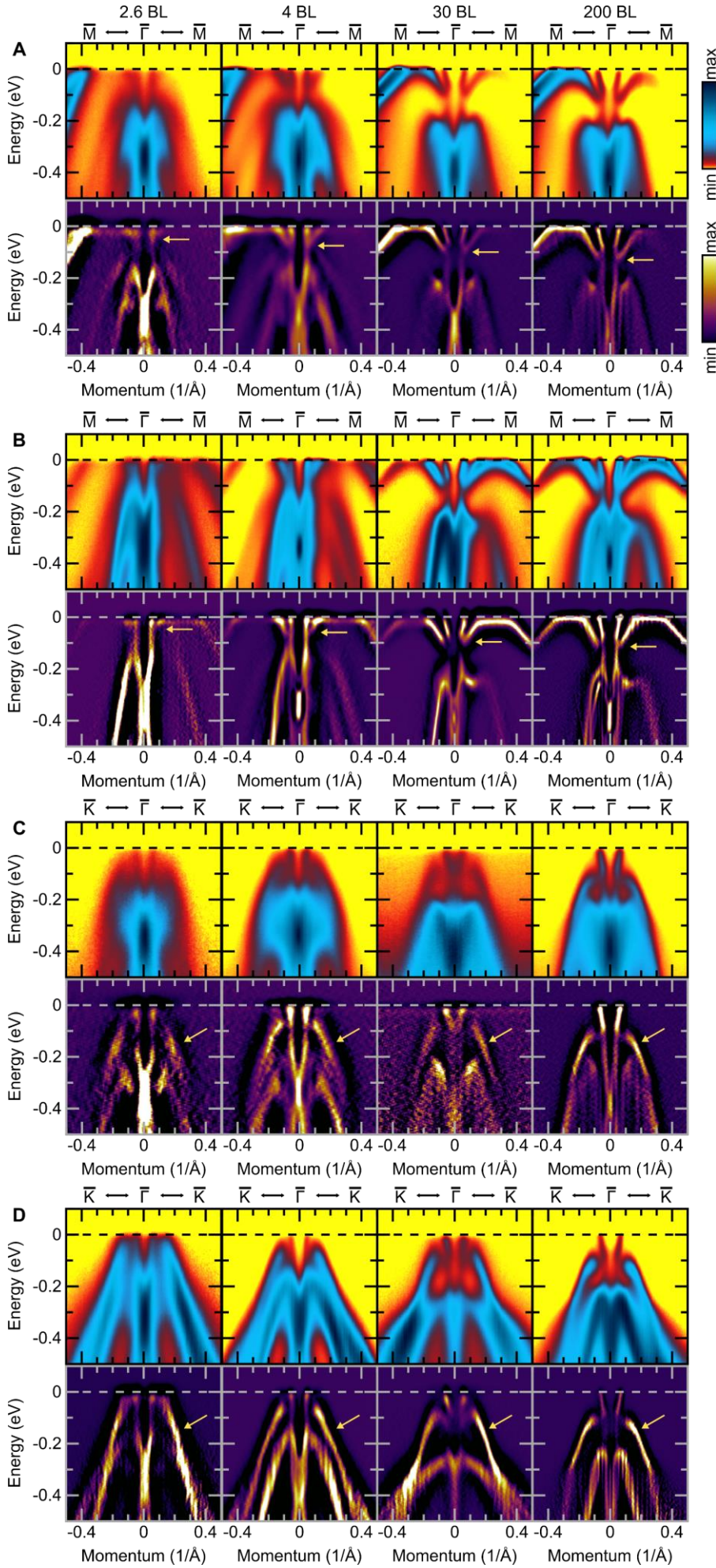


Fig. S4. ARPES spectra of Bi films near $\bar{\Gamma}$, highlighting the surface state band energy shift. ARPES images of the raw spectra (top panels) and 2D curvature plots (bottom panels), enhancing the dispersive band features. (A and B) $\bar{M} - \bar{\Gamma} - \bar{M}$ and (C and D) $\bar{K} - \bar{\Gamma} - \bar{K}$ cuts collected at an incident photon energy (A and C) $h\nu = 37.5$ eV and (B and D) $h\nu = 20$ eV. In (A and B) the surface state band minimum energy for each film thickness is highlighted with an arrow. In (C and D) the change in the surface state band dispersion to a more linear-like E - k dispersion is highlighted with an arrow.

In Fig. S4, high-resolution photoemission scans near $\bar{\Gamma}$ are collected at 20 and 37.5 eV photon energies, which should be close to the bulk Γ and T points, respectively, assuming an inner potential of 6-10 eV. No surface state dispersion is observed as a function of photon energy, yet the scans collected at 30 – 40 eV show a higher surface state cross-section and are more bulk sensitive (i.e., show the 3-fold symmetry near \bar{M}) than scans collected at 20 eV. The surface state energy minimum in the $\bar{M} - \bar{\Gamma}$ direction is monitored as a function of film thickness, showing a shift towards the Fermi level with decreasing film thickness (Fig. S4A-B). Moreover, as the film thickness decreases, the bottom surface state band along $\bar{K} - \bar{\Gamma}$ evolves into a more linear-like dispersion. No additional surface states (from the Bi-InSb interface) are observed in the $\bar{K} - \bar{\Gamma}$ direction for any of the films thicker than 1.3 BL.

ARPES spectra of a 1.3 BL thick Bi film in Fig. S5 show no evidence of InSb bulk or surface bands (see Fig. S2) in any of the cuts along the $\bar{M} - \bar{\Gamma} - \bar{M}$ or $\bar{K} - \bar{\Gamma} - \bar{K}$ directions, in contrast to the 1 BL Bi films grown on Bi_2Te_3 showing strong hybridization between the film and the underlying substrate [23,26]. While the bands are slightly more diffused due to the absence of long-range order in ~ 1 BL films (Fig. 2E), we observe the Bi-vacuum surface states crossing the Fermi level along $\bar{M} - \bar{\Gamma} - \bar{M}$, similar to thicker films. Along $\bar{K} - \bar{\Gamma} - \bar{K}$ in Fig. S5(G-H) we see an additional surface state band which we suspect originates at the Bi-InSb interface and was also predicted by our DFT calculations.

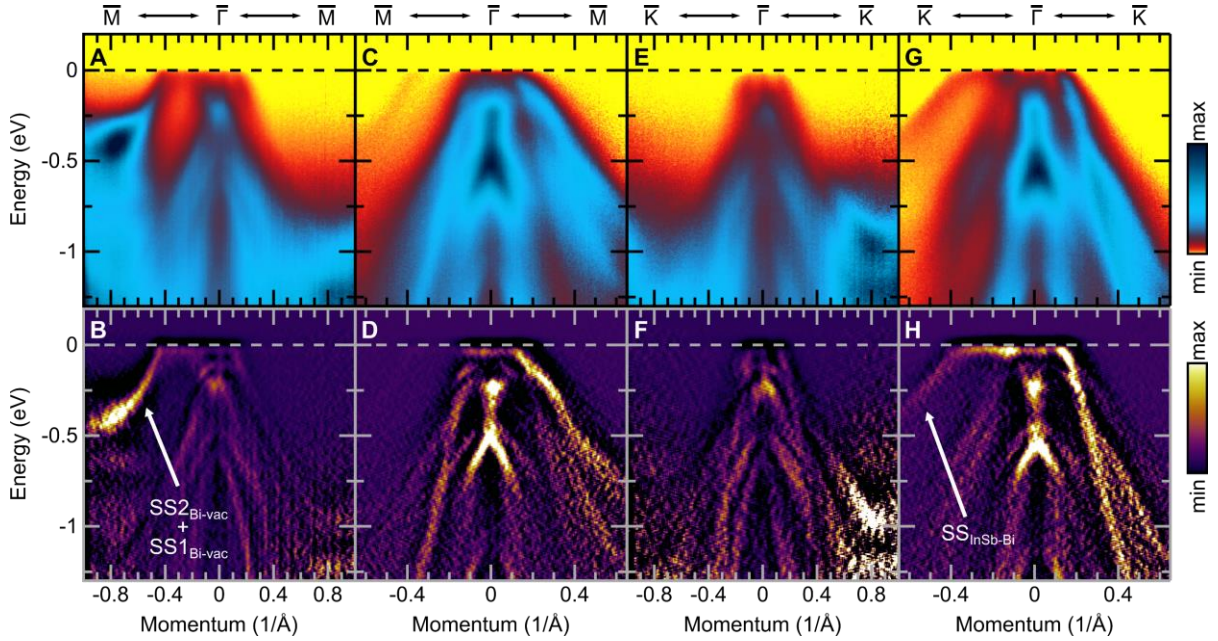


Fig. S5. ARPES spectra of a 1.3 BL thick Bi film. ARPES images of the raw spectra (top panel) and 2D curvature plots (bottom panel) enhancing the dispersive band features. (A-D) $\bar{M} - \bar{\Gamma} - \bar{M}$ cuts collected at a photon energy of (A-B) $h\nu = 37.5$ eV and (C-D) $h\nu = 20$ eV. (E-H) $\bar{K} - \bar{\Gamma} - \bar{K}$ cuts collected at photon energy of (E-F) $h\nu = 37.5$ eV and (G-H) $h\nu = 20$ eV. The two surface states (indistinguishable due to their overlap) at the Bi-vacuum interface are highlighted in (B). The surface state originating at the Bi-InSb interface is highlighted in (H).

Additional DFT calculations

We investigated the electronic structure of bulk InSb (see Fig. S2B) using screened hybrid functional of Heyd, Scuseria, and Ernzerhof (HSE06) [62,63] with 25% of exact exchange and accounting for spin-orbit coupling. A Γ -centered $6 \times 6 \times 6$ k-point mesh was employed in the InSb bulk band structure calculations to optimize the lattice parameters and the self-energy.

We calculated the band structure of freestanding Bi ultrathin films where we allowed the in-plane lattice parameter to relax, and see a decrease in the lattice parameter as the film thickness decreases: $a_{\text{Bi,relaxed}}^{\text{freestanding}} = 4.264, 4.402, 4.441, 4.463, 4.475, \text{ and } 4.484 \text{ \AA}$ for 1, 2, 3, 4, 5, and 6 BL thick films, respectively. This contraction in the lattice parameter for the freestanding film is consistent with earlier studies of ultrathin Bi films [45].

To confirm strong interfacial bonding, we also let the in-plane lattice parameter of the Bi/InSb films relax (presented in Fig. S6). The lattice parameter of the 1-6 BL Bi films on InSb gradually decreases, approaching the Bi bulk lattice parameter with increasing film thickness: $a_{\text{Bi,relaxed}}^{\text{Bi/InSb}} = 4.603, 4.607, 4.597, 4.592, 4.588, 4.583 \text{ \AA}$ for 1-6 BL thick films, respectively. The band structure of the relaxed Bi/InSb films is very similar to the in-plane-constrained structures in Fig. 4B when comparing band dispersion and quantum-well energies at \bar{M} (within a 20 meV energy difference, see Fig. S6). Thus, the \mathbb{Z}_2 trivial topological band assignment is not heavily dependent on the relaxed/strained ranges for ultrathin films of Bi/InSb.

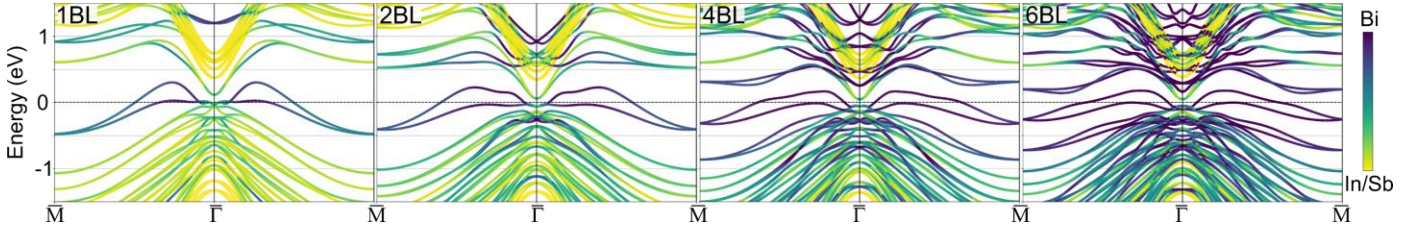


Fig. S6. DFT calculations along $\bar{M} - \bar{\Gamma} - \bar{M}$ of the relaxed Bi/InSb (111) structure. States with more than 60% of their weight in the Bi film are marked in purple, and states with 0% of their weight in the Bi film (originating from the InSb layer) are marked in yellow.

We have also investigated BL-resolved DFT calculations for the topological trivial and nontrivial cases of the Bi/InSb structures in Fig. S7 to highlight the difference in the intensity of bands originating from the top and bottom layers in inversion asymmetric films based on band topology. This treatment follows earlier detailed studies performed on other inversion asymmetric structures [11,37,47]. To accurately determine the layer-resolved band origin, we have focused on the region near the surface Brillouin zone center due to the higher localization of surface state bands and their reduced penetration into the film bulk [35]. In both cases, the Bi film has the same in-plane lattice constant fixed to the computed InSb lattice parameter of $a_{Bi, fixed}^{Bi/InSb} = a_{[110]}^{InSb} = 4.628 \text{ \AA}$, and the same Bi-InSb interfacial distance. The Bi film with a trivial band structure has an out-of-plane lattice constant of $c_{Bi}^{bulk} = 11.709 \text{ \AA}$ and the \mathbb{Z}_2 nontrivial band topology was modeled by fixing the out-of-plane lattice parameter to a relatively high value of $c_{Bi}^{nontrivial} = 1.15 \times c_{Bi}^{bulk} = 13.465 \text{ \AA}$ to ensure a transition to a \mathbb{Z}_2 nontrivial band topology based on earlier reports modeling the inversion gap at L [1,37,48].

Surface states from opposite interfaces will still leak to the adjacent interface at a thickness of 6 BL, however their origin can be distinguished based on the relative changes in band localization. In the \mathbb{Z}_2 nontrivial case, Fig. S7(A and B), we observe a strong intensity of two surface state pairs labeled (i) a and a' and (ii) b and b'. A third pair of bands with weaker intensities was observed to cross the Fermi level near $k \sim 0.25 \text{ 1/\AA}$ and was confirmed to have In/Sb atom contributions and was therefore assumed to be an InSb-related surface state. The pairs a and a' correspond to states localized at the top surface, and b and b' to states localized at the bottom BL. Each pair is expected to gap out at \bar{M} , though bands a and b, and bands a' and b' will each meet at \bar{M} as discussed at length in [37]. In the trivial band structure case in Fig. S7(C and D), we see only one pair of surface states intersecting the Fermi level in the top BL (Fig. S7D). The bottom BL in Fig. S7C shows no significant contributions from those surface states. The surface states at the top BL are confirmed to cross at \bar{M} , as shown in Fig. 4D.

The arrangement of the Bi atom positions on top of the InSb slab was studied via HSE calculations, showing only minor energy differences (ΔE) between three InSb-Bi stackings: C-A ($\Delta E = 0 \text{ meV}$), C-B ($\Delta E = 8.62 \text{ meV}$), and C-C ($\Delta E = 5.74 \text{ meV}$), with the InSb substrate following the conventional face-centered cubic A-B-C-A-B-C stacking. In the C-A stacking, the first Bi monolayer (lower plane of the buckled BL) lies vertically above the last layer of Sb atoms in the InSb slab. In the C-C stacking, that monolayer lies above the last layer of In atoms in the InSb slab. We present the DFT calculations performed for the C-A stackings, which agree better with the ARPES-measured binding energy scaling of quantum-well states with film thickness shown in Fig. 4E.

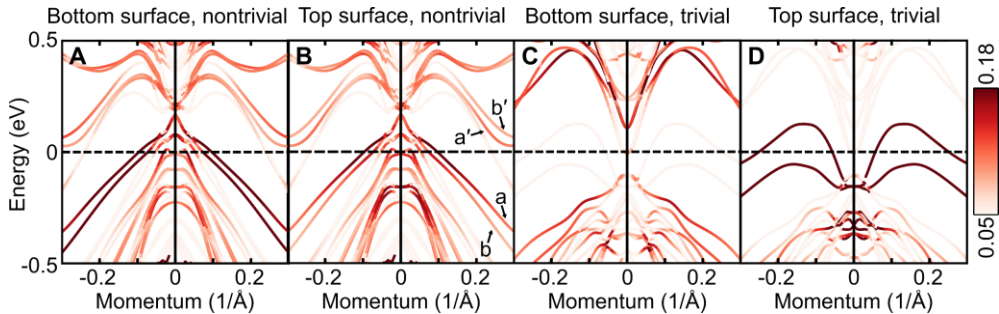


Fig. S7. DFT calculations along $\bar{M} - \bar{\Gamma} - \bar{M}$ near $\bar{\Gamma}$ for 6 BL thick Bi/InSb (111) films, for states localized at the top and bottom BLs of trivial and nontrivial band structures. The color scheme depicts the fraction of localization of a state at each surface, where the bottom BL in the Bi film is interfaced with InSb, and the top BL is at the film-vacuum interface. (A and B) The Bi/InSb band structure with the c-axis strained by 15% is predicted to have a \mathbb{Z}_2 nontrivial band topology. (C and D) The Bi/InSb band structure without strain in the c-axis, with a trivial \mathbb{Z}_2 band topology, the same structure as shown in Fig. 4D only for a narrower k range. (A and C) Bottom and (B and D) top BL-resolved bands. The surface state pairs for each interface in the nontrivial band structure are marked with letters (a and a', b and b').

Section S3

Phase accumulation model

The phase accumulation model [64–66] is derived directly from the Bohr-Sommerfeld quantization condition for the existence of a quantum-well state of a quantum number n :

$$2k_z d + \phi_{tot} = 2\pi(n - 1) \quad (1)$$

Where k_z is the wavevector perpendicular to the film plane, the film thickness, d , is the product of the number of BLs, N , and t is the BL thickness: $d = N * t$, $t = 3.95 \text{ \AA}$. The total phase shift, ϕ_{tot} , is the sum of the phase shifts at each interface: $\phi_{tot} = \phi_{Bi-vacuum} + \phi_{Bi-InSb}$.

In the ideal case of a quantum-well with infinite potential boundaries, we arrive at a standing wave solution: $\phi_{tot} = 2\pi n$, where each interface has a reflection of π . If the phase shift of a given interface is small and approaches 0, there is significant spilling of the electron density into the underlying substrate. The quantum-well states in Bi thin films observed at \bar{M} originate due to the quantization of the bulk band along the X-L direction. Along this path, the $E(k_z)$ band disperses nearly linearly up to a 1.5 eV binding energy (see Fig. 1); therefore, a linear approximation $E = \alpha k_z + \beta$ was suggested [8] to estimate the dispersion relation. Inserting equation (1) into this linear dependence, we arrive at [8]:

$$E = \alpha \left[\frac{2\pi(n-1) - \phi_{tot}}{2d} \right] + \beta = \frac{\alpha}{2Nt} [2\pi(n-1) - \phi_{tot}] + \beta \quad (2)$$

$$E \propto 0.487[2\pi(n-1) - \phi_{tot}] \frac{1}{N} \quad (2)$$

To find α , we extract k_z for multiple binding energies. Assuming ϕ_{tot} is only a function of the binding energy for the quantum numbers $n=2$, $n'=3$ [66], and by solving equation (1) for two different quantum-well states (n' , n) with the same binding energy but different film thicknesses (N' , N) (obtained by interpolating the linear curves- $E(N) = m \left(\frac{1}{N} \right) + c$ in Fig. 4E, see values in Table S1) we extract $k_z(E)$:

$$k_z(N', n') = k_z(N, n) \rightarrow k_z = \frac{\pi}{2t} \frac{n-n'}{N'-N} \quad (3)$$

And from the $E(k_z)$ relationship, we find that $\alpha = 3.85 \text{ eV \AA}$. From the linear slopes in Fig. 4E, we extract the total phase shift obtained for each quantum number:

$$2\pi(n-1) - \phi_{tot} = m \left(\frac{2t}{\alpha} \right) \rightarrow \phi_{tot}^{n=1} = 1.20\pi, \quad \phi_{tot}^{n=2} = 1.48\pi, \quad \phi_{tot}^{n=3} = 1.53\pi$$

The vacuum phase $\phi_{Bi-vacuum}$ is calculated using the Wentzel, Kramers, and Brillouin (WKB) approximation for a pure image potential [65]:

$$\phi_{Bi-vacuum} = \pi \left(\sqrt{\frac{3.4}{E_V - E}} - 1 \right) \quad (4)$$

Where the vacuum energy, E_V , with respect to the Fermi level, is the film's work function (WF), $WF=4.34 \text{ eV}$ [67]. Therefore, near the Fermi level at a binding energy $E = -0.15 \text{ eV}$: $\phi_{Bi-vacuum} = -0.13 \text{ eV}$, and the phase shift at the Bi-InSb interface is:

$$\phi_{Bi-InSb}^{n=1} = 1.33\pi, \quad \phi_{Bi-InSb}^{n=2} = 1.61\pi, \quad \phi_{Bi-InSb}^{n=3} = 1.66\pi$$

Table S1. DFT-calculated and ARPES-extracted binding energies of quantum-well states $n=1,2,3$ at \bar{M} for the Bi films

# of DFT calculated BLs	Binding Energy (eV)		
	n=1	n=2	n=3
1	-0.442	-1.047	-1.291
2	-0.381	-1.002	-1.239
3	-0.323	-0.923	-1.178
4	-0.277	-0.842	-1.132
5	-0.253	-0.763	-1.080
6	-0.214	-0.696	-1.022
# of ARPES measured BLs			
1.25	-0.412	-1.00	-1.4
2.63	-0.324	-0.940	-1.27
4	-0.24	-0.782	-1.175
5.38	-0.203	-0.647	-1.034
7.87	-0.175	-0.510	-0.750
13	-0.116	-0.323	-0.529
30	-0.049	-0.166	-0.280
200	-0.03	-0.03	-0.03